



**HAL**  
open science

## Cooling patterns in rotating thin spherical shells - Application to Titan's subsurface ocean

Hagay Amit, Gael Choblet, G. Tobie, Filipe Terra-Nova, Ondřej Čadek,  
Mathieu Bouffard

► **To cite this version:**

Hagay Amit, Gael Choblet, G. Tobie, Filipe Terra-Nova, Ondřej Čadek, et al.. Cooling patterns in rotating thin spherical shells - Application to Titan's subsurface ocean. *Icarus*, 2020, 338, pp.113509. 10.1016/j.icarus.2019.113509 . hal-02371953

**HAL Id: hal-02371953**

**<https://hal.science/hal-02371953>**

Submitted on 21 Dec 2021

**HAL** is a multi-disciplinary open access archive for the deposit and dissemination of scientific research documents, whether they are published or not. The documents may come from teaching and research institutions in France or abroad, or from public or private research centers.

L'archive ouverte pluridisciplinaire **HAL**, est destinée au dépôt et à la diffusion de documents scientifiques de niveau recherche, publiés ou non, émanant des établissements d'enseignement et de recherche français ou étrangers, des laboratoires publics ou privés.



Distributed under a Creative Commons Attribution - NonCommercial 4.0 International License

# Cooling patterns in rotating thin spherical shells – application to Titan’s subsurface ocean

Hagay Amit<sup>a</sup>, Gaël Choblet<sup>a</sup>, Gabriel Tobie<sup>a</sup>, Filipe Terra-Nova<sup>a,b</sup>,  
Ondřej Čadek<sup>c</sup>, Mathieu Bouffard<sup>d</sup>

September 26, 2019

<sup>a</sup> CNRS UMR 6112, Université de Nantes, Laboratoire de Planétologie et de Géodynamique,  
2 rue de la Houssinière, Nantes, F-44000, France

<sup>b</sup> Departamento de Geofísica, Instituto de Astronomia, Geofísica e Ciências Atmosféricas,  
Universidade de São Paulo, Rua do Matão, 1226, Cidade Universitária, 05508-090 São Paulo,  
Brazil

<sup>c</sup> Charles University, Faculty of Mathematics and Physics, Department of Geophysics, V  
Holešovičkách 2, 18000 Prague, Czech Republic

<sup>d</sup> Max Planck Institute for Solar System Research, Justus-von-Liebig-Weg 3, 37077 Göttingen,  
Germany

E-mail address: Hagay.Amit@univ-nantes.fr (H. Amit).

*Revised for Icarus (deleted text ~~erossed~~, added text **in bold**)*

## Abstract

We use rotating convection simulations in a thin spherical shell to study fluid dynamics in subsurface oceans of icy moons. We find two types of persistent results, characterized by larger outer boundary heat flux either at polar regions or at the equatorial region. Simulations corresponding to larger Rossby numbers result in polar cooling with moderate lateral heterogeneity in heat flux, whereas lower Rossby numbers give equatorial cooling

22 with more pronounced heat flux heterogeneity. The polar cooling scenario is in agreement  
23 with inferences for the heat flux at the top of Titan’s ocean, which may provide a dynamical  
24 constraint for the vigor of convection in this layer. Our results may help unraveling the  
25 internal dynamics and the interactions among the different layers within the hydrosphere  
26 of Titan. Possible implications for the deep interiors of other icy moons are envisaged.

## 27 **1 Introduction**

28 Many water rich planetary bodies in the outer solar system are considered to be ”ocean worlds”  
29 in the sense that these bodies likely harbor global layers of liquid water beneath their surface  
30 ice shells (cf. e.g. Nimmo and Pappalardo, 2016). Early inferences for the possible pres-  
31 ence of internal oceans buried in distant moons relied on thermal evolution models (in the  
32 case of Jupiter’s satellites Ganymede and Europa, for example, cf. Kirk and Stevenson, 1987;  
33 Ojakangas and Stevenson, 1989). Geophysical measurements by the Galileo and Cassini-  
34 Huygens missions involved various techniques for detecting buried oceans. Owing to Jupiter’s  
35 detectable dipole tilt, magnetic induction enabled to identify global scale conductive layers in  
36 the major icy moons orbiting in the magnetosphere, most notably Europa (Zimmer et al., 2000;  
37 Khurana et al., 2002). For Ganymede, a more ambiguous measurement due to the presence of  
38 an internal dynamo (Kivelson and Khurana, 2002) was later confirmed by Earth-based obser-  
39 vation of auroral oscillations (Saur et al., 2015). In the system of Saturn, evidence for internal  
40 oceans was found at three moons, Titan, Enceladus and Mimas, and internal oceans are sus-  
41 pected in two other moons, Dione and Rhea. For Titan, the presence of an internal ocean was  
42 confirmed by three independant observations: electric signals measured by the Huygens probe  
43 during its descent through Titan’s atmosphere **atmosphere** (Béghin et al., 2010, 2012), obliquity  
44 three times larger than expected (Baland et al., 2011, 2014) and gravitationnal tides (Iess  
45 et al., 2010; Mitri et al., 2014). For Mimas and Enceladus, the existence of a global ocean was  
46 determined from the detection of libration (Tajeddine et al., 2014; Thomas et al., 2016). For  
47 Mimas, the observed libration could also be explained by a very elongated rocky core, so that  
48 the existence of an ocean is not certain (Tajeddine et al., 2014). In the case of Enceladus, the  
49 existence of a global ocean is also consistent with the observed topography and graviy fields  
50 (Čadek et al., 2016; Beuthe et al., 2016; Hemingway et al., 2018). Such oceans constitute

51 at present some of the most promising of potentially habitable extraterrestrial environments  
52 and two ambitious planetary missions to come are devoted to their characterization: ESA's  
53 JUICE scrutinizing Ganymede (Grasset et al., 2013) and NASA's Europa Clipper (Phillips and  
54 Pappalardo, 2014).

55 Observations of non-water compounds at Europa's surface (McCord et al., 2002; Ligier  
56 et al., 2016) and in ejected icy grains at Enceladus (Postberg et al., 2009, 2011; Hsu et al.,  
57 2015, 2018) suggest chemical transport from the ocean seafloor up to the surface. However,  
58 the practical means by which the oceans convey this signature are uncertain. Convection in  
59 Europa's buried ocean was considered in the light of localized heating at its seafloor in a  
60 weakly stratified ocean (Thomson and Delaney, 2001). Their scaling analysis of rotationally  
61 confined instabilities is further constrained by dedicated experiments (Goodman et al., 2004).  
62 Vance and Goodman (2009) set such mechanisms in the more general context of an uncertain  
63 European oceanography, including global scale convecting and rotating flow. Double diffusive  
64 convection is also envisioned (Vance and Brown, 2005).

65 **Although often with a thick shell in the context of Earth's outer core, the pattern**  
66 **of convection and heat transport in rapidly rotating spherical shells at onset and their**  
67 **dependence on control parameters have been thoroughly explored (for a review see e.g.**  
68 **Aurnou et al., 2015). Dormy et al. (2004) identified the onset of convection at the edge of**  
69 **the tangent cylinder for any spherical shell thickness. Zhang and Jones (1993) found that**  
70 **an Ekman boundary layer that is formed where axial convective rolls impinge the outer**  
71 **boundary destabilizes/stabilizes convection when viscous/thermal dissipation dominates,**  
72 **respectively. Tilgner and Busse (1997) observed that when convection vigor is enhanced**  
73 **the heat transport across the shell increases, in particular at polar regions. Gastine et al.**  
74 **(2016) conducted a systematic parametric study of convection in a rotating spherical**  
75 **shell of aspect ratio 0.6. They established scaling laws that separate different convective**  
76 **regimes.**

77 ~~To our best knowledge, the sole attempt to date at modeling Soderlund et al. (2014) mod-~~  
78 ~~elled rotating convection in a thin 3D spherical shell for a subsurface ocean. was proposed~~  
79 ~~by Soderlund et al. (2014) who~~ **They** found latitudinal dependence of heat transfer. In the case

80 of Europa, this effect may explain the preferred occurrence of specific surface features (chaos  
81 terrains, salt deposits) at moderate latitudes. In thin, rapidly rotating ocean shells the outer  
82 boundary heat flux is expected to be concentrated at low latitudes (Miquel et al., 2018). Other  
83 efforts to relate the global ice shell structure of ocean worlds to ocean dynamics have focused  
84 on ice shell melting, e.g. in the case of European chaos-type features (Thomson and Delaney,  
85 2001), Titan (Kvorka et al., 2018) or Enceladus (Čadek et al., 2019), but the possible lessons  
86 on ocean dynamics and heat transfer are only preliminary.

87 In this context, we follow the approach initiated by Soderlund et al. (2014) to better char-  
88 acterize the ~~poorly known~~ dynamics of buried oceans at a global scale. We present simulations  
89 of thermal convection of a rotating fluid in a thin spherical shell for a range of control param-  
90 eters. We focus on the resulting heat flux pattern at the top of the shell. Due to computational  
91 limitations (e.g. Glatzmaier, 2002) the explored control parameters are very remote from the  
92 actual values in buried oceans - some projections of our results thus require extrapolation (as  
93 is the case for most rapid rotation applications, cf. Aubert et al., 2017).

94 The paper is outlined as follows. In section 2 we detail our method. Our results are ana-  
95 lyzed in section 3. We place our models in the expected dynamical regime based on previous  
96 literature (section 4) and then compare the results from our simulations to inferences from  
97 Cassini’s observations for the heat flux at the top of Titan’s ocean (section 5). Finally, we  
98 discuss the main results and their implications for Titan’s ocean (section 6).

## 99 **2 Method**

100 We simulate rotating convection in a thin spherical shell. **The impact of the shell thick-**  
101 **ness on the convection style is not trivial. In the case of rapidly rotating models, Miquel**  
102 **et al. (2018) found that the determining parameter to characterize the vigor and extent**  
103 **of low-latitude convective trapping combines the geometry and rotational effects. When**  
104 **thermal forcing is enhanced, convection emerges inside the tangent cylinder (e.g. Tilgner**  
105 **and Busse, 1997), hence the shell thickness which dictates the surficial extent of the tan-**  
106 **gent cylinder becomes an important factor. Deep liquid systems encompass a variety of**

107 **shell thicknesses; In Table 1 we list the shell thicknesses and the corresponding relative**  
108 **tangent cylinder surfaces of some of these systems.** Here we term a shell "thin" as one that  
109 its inner to outer radii ratio  $r_i/r_o$  is significantly larger than e.g. that of Earth's outer core  
110 **resulting in a relative tangent cylinder surface about an order of magnitude larger than**  
111 **that of Earth's outer core.**

System	$r_i/r_o$	$S^h/S$	Reference
Mercury's core	0.15 – 0.50	0.01 – 0.13	Hauck et al. (2018)
Earth's core	0.35	0.06	Dziewonski and Anderson (1981)
Titan's ocean	0.84 – 0.96	0.46 – 0.72	Vance et al. (2018)
Enceladus' ocean	0.78 – 0.90	0.37 – 0.56	Čadek et al. (2019)
Europa's ocean	0.92 – 0.94	0.61 – 0.66	Vance et al. (2018)
Pluto's ocean	0.94	0.66	Gabasova et al. (2018)
Our models	0.8	0.4	

Table 1: Deep liquid systems, their aspect ratio and relative tangent cylinder surface. Ranges for Mercury's core are based on combinations of the first and third quartiles of Hauck et al. (2018), see their Table 5. For comparison we give the values for our models in the last line.

112 The numerical models solve the following set of self-consistent non-dimensional Boussi-  
113 nesq hydrodynamics equations for thermal convection of a fluid in a rotating spherical shell:

$$E \left( \frac{\partial \vec{u}}{\partial t} + \vec{u} \cdot \nabla \vec{u} - \nabla^2 \vec{u} \right) + 2\hat{z} \times \vec{u} + \nabla P = Ra^* \frac{\vec{r}}{r_o} T \quad (1)$$

$$\frac{\partial T}{\partial t} + \vec{u} \cdot \nabla T = \frac{1}{Pr} \nabla^2 T \quad (2)$$

$$\nabla \cdot \vec{u} = 0, \quad (3)$$

116 where  $\vec{u}$  is the velocity,  $T$  is temperature,  $t$  is time,  $\hat{z}$  is a unit vector in the direction of the  
117 rotation axis,  $P$  is pressure and  $\vec{r}$  is the position vector. Three non-dimensional parameters in  
118 (1) - (3) control the dynamics. The modified Rayleigh number  $Ra^*$  represents the strength of  
119 buoyancy force driving the convection relative to retarding forces

$$Ra^* = \frac{\alpha g_0 \Delta T D}{\nu \Omega}, \quad (4)$$

120 where  $\alpha$  is thermal expansivity,  $g_0$  is gravitational acceleration on the outer boundary at radius  
121  $r_o$ ,  $\Delta T$  is the fixed temperature difference between the inner and outer boundaries,  $D$  is shell

122 thickness,  $\nu$  is kinematic viscosity and  $\Omega$  is the rotation rate. The Ekman number represents  
 123 the ratio of viscous and Coriolis forces

$$E = \frac{\nu}{\Omega D^2}. \quad (5)$$

124 The Prandtl number is the ratio of kinematic viscosity to thermal diffusivity

$$Pr = \frac{\nu}{\kappa}, \quad (6)$$

125 where  $\kappa$  is thermal diffusivity. The modified Rayleigh number  $Ra^*$  is related to the conven-  
 126 tional Rayleigh number by  $Ra^* = Ra \cdot E/Pr$ , where the conventional Rayleigh number  $Ra$  is  
 127 given by

$$Ra = \frac{\alpha g_0 \Delta T D^3}{\nu \kappa}. \quad (7)$$

128 To dimensionalize the solutions velocity is scaled by  $D/\nu$ , time by  $D^2/\nu$  and temperature by  
 129  $\Delta T$ .

130 Some relevant output parameters are monitored. The Reynolds number which represents  
 131 the ratio of inertial to viscous forces is calculated based on the rms velocity  $U$  in the volume  
 132 of the shell

$$Re = \frac{UD}{\nu} \quad (8)$$

133 and the Rossby number represents the ratio of inertial to Coriolis forces

$$Ro = \frac{U}{\Omega D} = Re \cdot E. \quad (9)$$

134 The magnitude of the heat flux anomaly on the outer (or inner) boundary  $q_o^*$  (or  $q_i^*$ ) is  
 135 defined as the ratio of the peak-to-peak amplitude of the zonal part of the heat flux to twice the  
 136 mean heat flux:

$$q^* = \frac{q_{max}^z - q_{min}^z}{2q_0}, \quad (10)$$

137 where  $z$  **superscript zonal** corresponds to **”zonal”**, i.e. averaging over latitude lines. This  
 138 definition differs from the more common definition based on the 2D heat flux distribution  
 139 and applied to large-scale input patterns (e.g. Olson and Christensen, 2002), while alternative  
 140 definitions were used for localized patterns (for a review see Amit et al., 2015). Here we use

141 the zonal heat flux in order to avoid bias from small-scale longitudinal variability which might  
 142 arise solely due to the finite simulation time of the runs.

143 The tangent cylinder effect is also quantified. We calculate the normalized difference be-  
 144 tween the time-average outer boundary heat flux inside to outside the tangent cylinder as fol-  
 145 lows:

$$\langle q_o \rangle^{h/l} = \frac{\langle q_o \rangle^h - \langle q_o \rangle^l}{\langle q_o \rangle^h + \langle q_o \rangle^l}, \quad (11)$$

146 where the mean heat flux inside the tangent cylinder, denoted by  $h$  superscript (for higher  
 147 latitudes), is

$$\langle q_o \rangle^h = \frac{1}{2S^h} \left( \int_0^{2\pi} \int_0^{\theta_{tc}} q_o(\phi, \theta) dS + \int_0^{2\pi} \int_{\pi-\theta_{tc}}^{\pi} q_o(\phi, \theta) dS \right) \quad (12)$$

148 and the mean heat flux outside the tangent cylinder, denoted by  $l$  superscript (for lower lati-  
 149 tudes), is

$$\langle q_o \rangle^l = \frac{1}{S^l} \int_0^{2\pi} \int_{\theta_{tc}}^{\pi-\theta_{tc}} q_o(\phi, \theta) dS. \quad (13)$$

150 In (12)-(13)  $S^h$  and  $S^l$  are the outer boundary spherical surface areas inside and outside the  
 151 tangent cylinder respectively,  $\theta_{tc}$  is the co-latitude where the tangent cylinder intersects the  
 152 outer boundary in the northern hemisphere given by  $\sin \theta_{tc} = r_i/r_o$  and the spherical surface  
 153 increment is  $dS = r^2 \sin \theta d\phi d\theta$  (**for a schematic illustration see Fig. 1**). The ratio  $\langle q_o \rangle^{h/l}$   
 154 (11) has some desired properties. For polar/equatorial cooling it is positive/negative respec-  
 155 tively, i.e. its sign indicates which cooling dominates. In addition, if one of the two coolings is  
 156 much stronger  $\langle q_o \rangle^{h/l}$  will approach  $\pm 1$  whereas if the two coolings are comparable it will  
 157 approach zero, i.e. its magnitude reflects the amplitude of the tangent cylinder effect.

158 The transition to a more turbulent regime may be marked by different non-dimensional  
 159 numbers (see Soderlund et al., 2014, and references therein). Apart from the conventional  
 160 Rossby number  $Ro$  (9), alternatives include the convective Rossby number

$$Ro_c = \left( \frac{RaE^2}{Pr} \right)^{1/2}, \quad (14)$$

161 the local convective Rossby number

$$Ro_{loc} = Ra^{5/4} E^2 \quad (15)$$

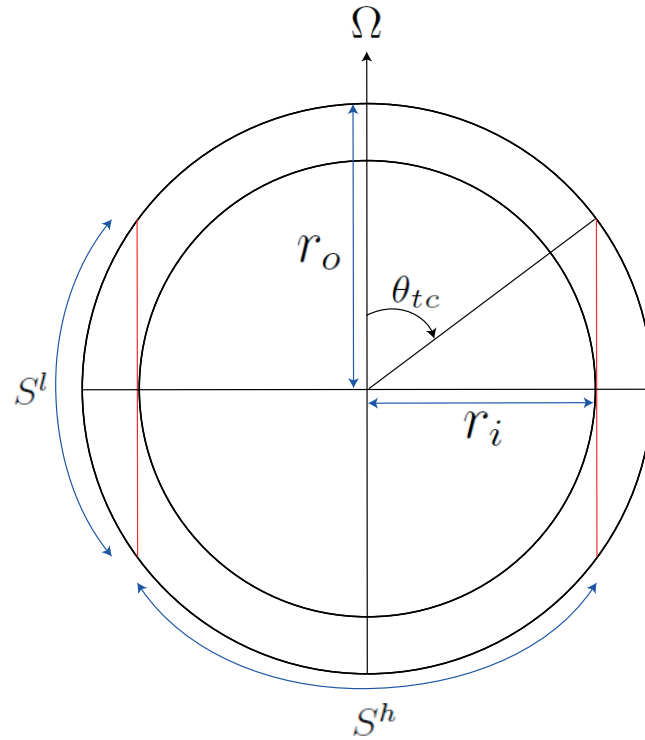


Figure 1: Schematic illustration of the tangent cylinder geometry. The rotation rate  $\Omega$  denotes the rotation axis, the horizontal line is the equatorial plane, red vertical lines denote the tangent cylinder.  $r_i$  and  $r_o$  are the inner and outer radii, respectively,  $\theta_{tc}$  is the co-latitude where the tangent cylinder intersects the outer boundary in the northern hemisphere,  $S^h$  and  $S^l$  are the outer boundary spherical surface areas inside and outside the tangent cylinder, respectively (represented by arcs in this schematic cross-section).

162 and a ratio representing a competition between thermal and rotational boundary layers

$$Ra/Ra_T = 0.1RaE^{3/2} \quad (16)$$

163 where  $Ra_T$  is a transitional Rayleigh number in water.

164 We use the code MAGIC by Johannes Wicht (Wicht, 2002). We analyze hydrodynamic (i.e.  
 165 non-magnetic) models with rigid isothermic **isothermal** boundary conditions. We focus on the  
 166 dynamics in relatively thin shells which are relevant for subsurface oceans of icy satellites. A  
 167 summary of model control parameters, geometries and some output parameters is given in  
 168 Table 2.

Case	$r_i/r_o$	$E$	$Ra$	$Ra/Ra_c$	$\ell_{max}$	$n_r$	$Ro_c$	$Ro_{loc}$	$Ra/Ra_T$	$Re$	$Ro$	Duration
1	0.7	$1 \cdot 10^{-3}$	$2 \cdot 10^5$	50.1	64	49	0.45	4.2	0.63	40	0.040	73
2	0.8	$1 \cdot 10^{-3}$	$2 \cdot 10^5$	35.0	64	49	0.45	4.2	0.63	48	0.048	45
3	0.8	$1 \cdot 10^{-3}$	$1 \cdot 10^6$	174.9	64	49	1	31.6	3.2	170	0.170	58
4	0.8	$1 \cdot 10^{-3}$	$3 \cdot 10^6$	524.8	64	49	1.7	124.9	9.5	335	0.335	52
5	0.8	$3 \cdot 10^{-4}$	$1 \cdot 10^6$	4.7	64	49	0.30	2.8	0.52	104	0.031	37
6	0.8	$3 \cdot 10^{-4}$	$1 \cdot 10^7$	47.1	64	49	0.95	50.6	5.2	523	0.157	36
7	0.8	$3 \cdot 10^{-4}$	$5 \cdot 10^7$	235.7	64	49	2.1	378.4	26.0	1273	0.382	35
8	0.8	$1 \cdot 10^{-4}$	$1 \cdot 10^7$	5.0	96	49	0.32	5.6	1	375	0.038	110
9	0.8	$1 \cdot 10^{-4}$	$2 \cdot 10^7$	10.0	96	49	0.45	13.4	2	638	0.064	94
10	0.8	$1 \cdot 10^{-4}$	$5 \cdot 10^7$	25.0	96	49	0.71	42.0	5	1140	0.114	98
11	0.8	$5 \cdot 10^{-5}$	$1 \cdot 10^7$	1.5	96	61	0.16	1.4	0.35	376	0.019	57

Table 2: Summary of models. **The critical Rayleigh number  $Ra_c$  was obtained using the open-source eigenmode solver Singe (Schaeffer, 2013; Vidal and Schaeffer, 2015), available at <https://bitbucket.org/nschaeff/singe>.** In all cases  $Pr = 1$ . The maximum spherical harmonic degree and order is  $\ell_{max}$  and the number of radial grid points in the shell is  $n_r$ . The duration of the simulations is given in **units** of advection time. Other control and output parameters are defined in the text.

169 Note that our control parameters are far from being realistic due to computational limita-  
 170 tions (e.g. Glatzmaier, 2002). In particular, the Ekman number in our models is far too large.  
 171 Recent geodynamo simulations have reached significantly smaller Ekman numbers (Aubert  
 172 et al., 2017; Schaeffer et al., 2017), though limited to relatively short runs. Our choice of  
 173 larger  $E$  values allows for sufficiently long simulations characterized by decent statistical con-  
 174 vergence towards meaningful time-average patterns. In addition, as we will show in the next

175 section, despite the relatively larger Ekman numbers our models cover the two endmember  
176 patterns of the outer boundary heat flux.

### 177 **3 Results**

178 Fig. 2 shows some images from an arbitrary snapshot of the large-scale case 1. Despite the  
179 large Ekman number, the moderate Rayleigh number leads to dynamics that is nevertheless  
180 affected by rotational effects. In our models convection is organized in equatorially symmetric  
181 axial columns (e.g. Taylor, 1917; Busse, 1970). This is evident in the form of north-south  
182 elongated radial vorticity (Fig. 2b) and heat flux (Fig. 2d) structures just below and on the  
183 outer boundary respectively, which result from deep meridional flow structures that are parallel  
184 to the rotation axis (Fig. 2c). The inner/outer radii ratio of 0.7 corresponds to a tangent  
185 cylinder intercepting the outer boundary at latitudes  $46^\circ$ . Indeed, the north-south elongated  
186 outer boundary heat flux and radial vorticity structures extend until about this latitude, while at  
187 higher latitudes convection is weaker. The axial convective columns and the tangent cylinder  
188 signature testify for the influence of rotation in the dynamics of this model.

189 Fig. 3 shows the same images for a long-term time-average of the same case. As expected,  
190 time-averaging smooths most of the small-scale longitudinal variability. The axial invariance  
191 of the flow (Fig. 3c) and the tangent cylinder effect (Fig. 3b) are clearly evident. The outer  
192 boundary heat flux is larger/lower at the equator/poles respectively (Fig. 3d), which we term  
193 "equatorial cooling" (following Heimpel and Evans, 2013).

194 The corresponding instantaneous and time-average distributions of inner boundary heat  
195 flux anomalies are given in Figs. 2e and 3e, respectively. The inner boundary heat flux anomaly  
196 is also positive at low-latitudes and negative at high-latitudes. The axial columnar flow touches  
197 the inner boundary in the equatorial plane and it is there where the heat is most effectively  
198 extracted from the inner boundary (Aubert et al., 2008). The approximately spherical harmonic  
199  $Y_2^0$  pattern is especially prominent in the time-average map (Fig. 3e). The same time-average  
200  $Y_2^0$  pattern was also found in numerical dynamo simulations with Earth-like core geometry and  
201 a somewhat different convection style (Aubert et al., 2008; Amit and Choblet, 2009). From

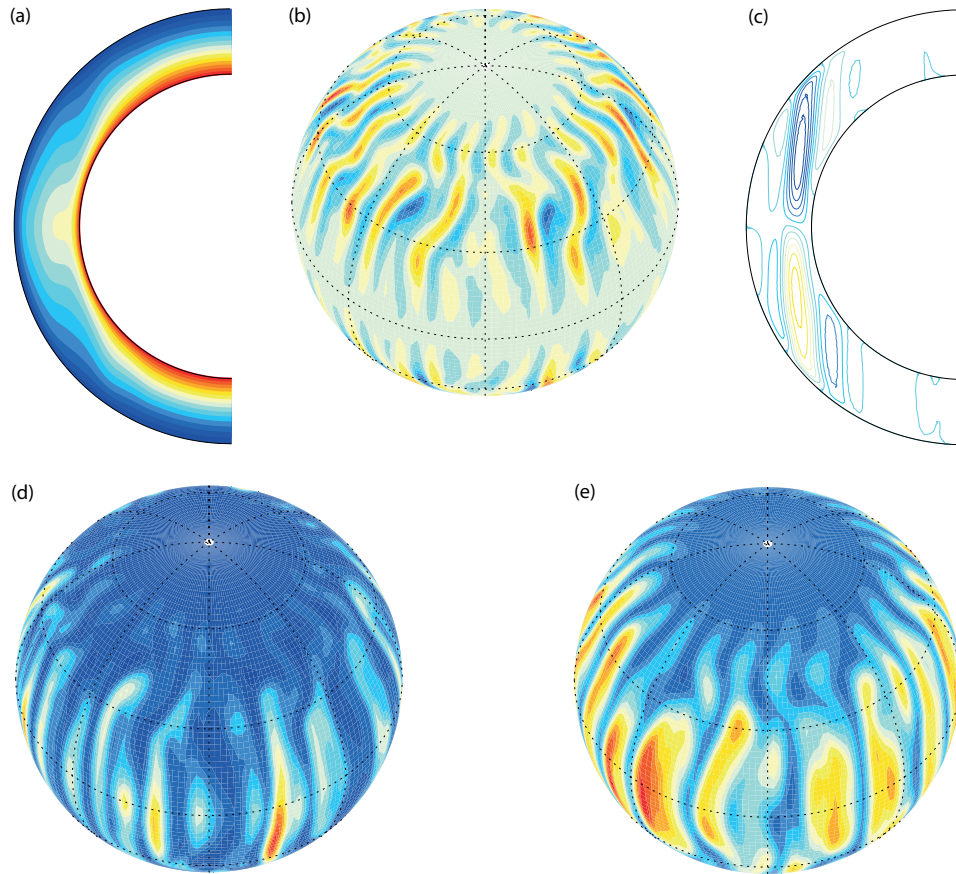


Figure 2: Images from a snapshot of case 1. (a) **Zonal Zonally-averaged** temperature; (b) Radial vorticity just below the outer boundary layer; (c) **Zonal Streamlines of the zonally-averaged** meridional flow; (d) Heat flux across the outer boundary; And (e) heat flux across the inner boundary. **In (a) red/blue denotes hot/cold respectively. In (b) red/blue denotes positive/negative radial vorticity, i.e. anti-clockwise/clockwise circulation, respectively.** In (c) red/blue contours denote anti-clockwise/clockwise circulation, respectively. In (d) and (e) red/blue denote positive/negative heat flux anomaly (i.e. heat flux with respect to the mean), respectively.

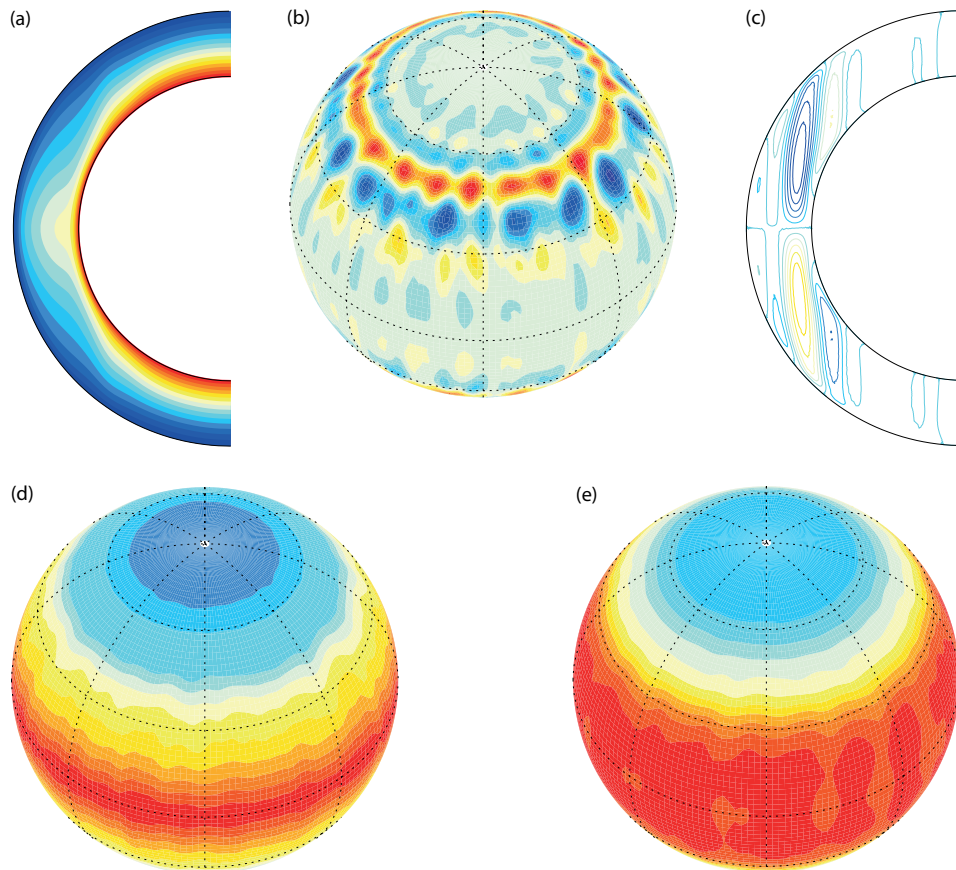


Figure 3: As in Fig. 2 for a long-term time-average of case 1, an example of equatorial cooling.

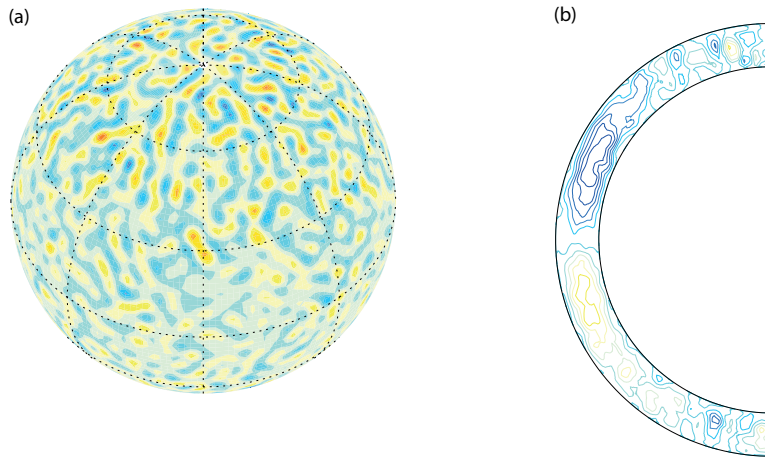


Figure 4: Images from a snapshot of case 10. (a) Radial vorticity just below the outer boundary layer; (b) Zonally-averaged meridional flow. Red/blue denotes anti-clockwise/clockwise circulation, respectively.

202 hereafter we focus on the time-average heat flux on both boundaries.

203 Rotational effects can be observed for a thinner shell as well. In all other cases the in-  
 204 ner/outer radii ratio is increased to 0.8. In this geometry the tangent cylinder intercepts the  
 205 outer boundary at lower latitudes,  $37^\circ$  in these cases. In addition, for the same control param-  
 206 eters convection is slightly stronger when confined to a thinner shell, resulting in a higher a  
 207 Reynolds number (compare cases 1 and 2 in Table 2) and thinner axial columns of instantane-  
 208 ous flow (not shown).

209 When convection is significantly stronger, the role of inertia in the dynamics may become  
 210 more important. In cases 9-10 the Rayleigh number is **more than a hundred** times larger  
 211 than in case 1. This results in a much larger  $Re$  and a larger  $Ro$  values (see Table 2) that  
 212 characterize a more turbulent flow. **The instantaneous axial convective rolls seen in case 1**  
 213 **(Figs. 2b and c) are broken and convective plumes fill the entire shell including inside the**  
 214 **tangent cylinder (Fig. 4).** The time-average outer boundary heat flux anomalies also exhibit  
 215 a  $Y_2^0$  pattern as in case 1, but perhaps surprisingly with an opposite sign (Fig. 5a), which we  
 216 term "polar cooling".

217 An intermediate cooling scenario is found in case 8. The outer boundary heat flux anomaly  
 218 is largest at the equator but also peaks at high latitudes with minima at mid latitudes, re-

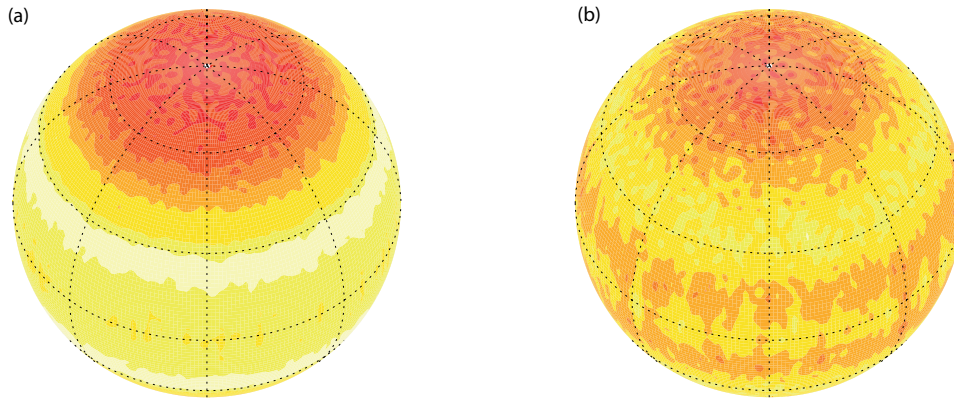


Figure 5: Heat fluxes for a long-term time-average of case 9, an example of polar cooling. (a) Across the outer boundary; (b) Across the inner boundary. **Red/blue denote positive/negative heat flux anomaly (i.e. heat flux with respect to the mean), respectively.**

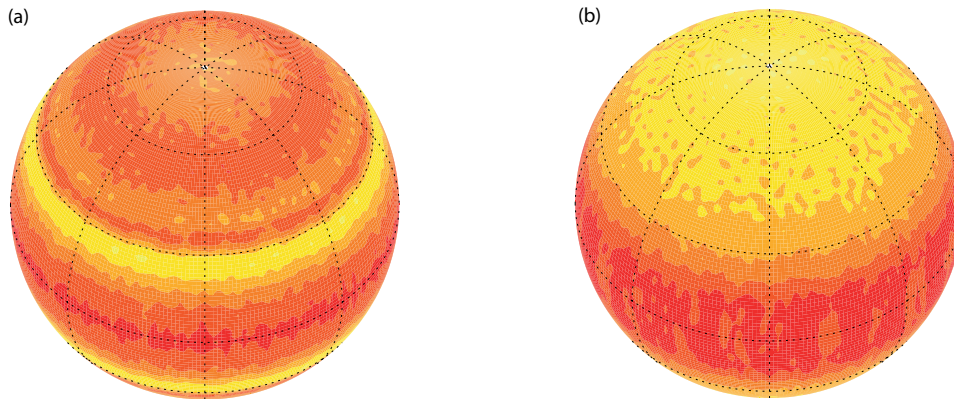


Figure 6: As in Fig. 5 for case 8, with intermediate cooling.

219 resembling spherical harmonic  $Y_4^0$  rather than  $Y_2^0$  (Fig. 6a). We term this more complicated  
 220 latitudinal dependence "intermediate cooling" (Table 3).

221 Figs. 3, 5 and 6 demonstrate that the runs are long enough to remove most of the transient  
 222 longitude-dependent features from the time-average patterns. This allows evaluating the results  
 223 in terms of their zonal profiles (Fig. 7). Comparing cases 1 and 2 which have the same control  
 224 parameters except for the shell thickness (Table 2), although the convective power depends on  
 225 both  $Ra$  and the shell thickness (e.g. Aubert et al., 2009), the tangent cylinder is distinguishable  
 226 between the two zonal outer boundary heat flux patterns. **In case 1 a change of trend appears**

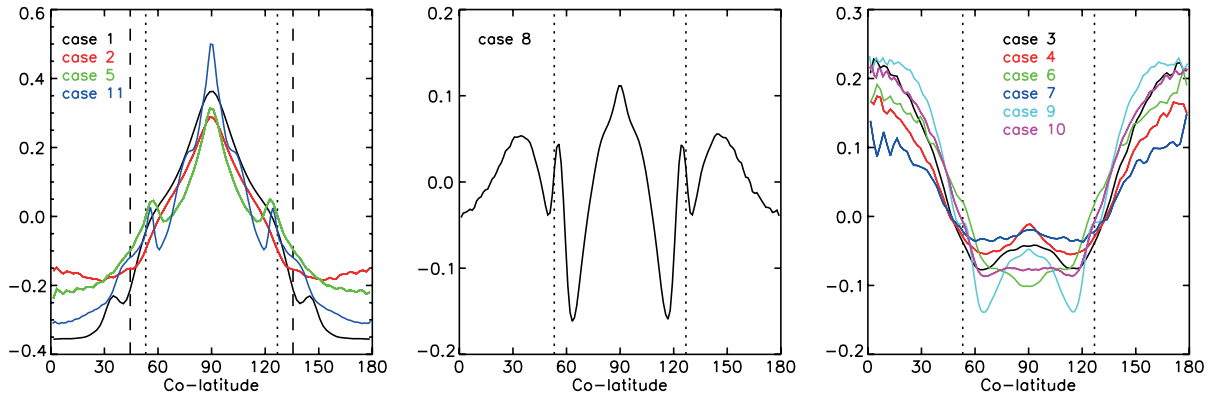


Figure 7: Non-dimensional ~~zonal~~ **zonally-averaged** outer boundary heat flux anomalies for the long-term time-averages of equatorial cooling cases (left), the intermediate cooling case 8 (middle) and polar cooling cases (right). The dashed vertical lines (left) denote the latitudes of the tangent cylinder in case 1, the dotted vertical lines denote the latitudes of the tangent cylinder in the other cases. Note the different scales.

227 **at higher latitudes (close to the dashed vertical line denoting the tangent cylinder in case**  
 228 **1) whereas in case 2 a change of trend appears at lower latitudes (close to the dotted**  
 229 **vertical line denoting the tangent cylinder in case 2).** In these cases equatorial cooling  
 230 prevails (Fig. 7 left and Table 3). Note the change of trend in the latitudinal dependence of  
 231 the heat flux in both cases, from steep outside to more moderate inside the tangent cylinder.  
 232 The other equatorial cooling cases 5 and 11 conform to this behavior as well, with the latter  
 233 exhibiting the strongest dichotomy between a peak equatorial to low polar heat flux (Fig. 7 left  
 234 and Table 3). Opposite trends characterize the polar cooling cases, with steep variation inside  
 235 the tangent cylinder and rather flat heat flux outside it (Fig. 7 right and Table 3). ~~Here there~~  
 236 ~~is less variability from one case to another.~~ Overall, the change in trend appears at somewhat  
 237 lower latitudes than that of the tangent cylinder. Finally, the intermediate case 8 does not fall  
 238 into any of the two categories (Fig. 7 middle and Table 3).

239 Table 3 and Figs. 8-9 summarize the results in terms of the parameter dependence of  
 240 the time-average mean heat flux, time-average amplitudes of heat flux heterogeneities and  
 241 the tangent cylinder effect. The mean outer and inner boundary heat fluxes increase with  
 242 increasing  $Ro_{loc}$  (Fig. 8a) as well as when other theoretical forms of the Rossby number  
 243 increase (Fig. 9a). **This is expected because increasing  $Ra$  leads to faster flow, larger**

244 **inertial effects and consequently larger heat flux.** Note that polar cooling (triangles) is  
 245 characterized by larger mean heat flux than equatorial cooling (diamonds). Around  $Ro_{loc} \sim$   
 246  $5 - 10$  (or corresponding critical values of  $Ro$ ,  $Ro_c$  and  $Ra/Ra_T$ ) the pattern shifts from  
 247 equatorial cooling for smaller values to polar cooling for larger values. In addition, decreasing  
 248 inertia results in decreasing heat flux spatial variability, i.e. polar cooling is characterized  
 249 by lower (relative) heat flux heterogeneities whereas equatorial cooling is characterized by  
 250 larger heat flux heterogeneities (Figs. 8b and 9b). This result is expected because when  $Ro$  is  
 251 increased the models approach the non-rotating regime in which the heat flux is homogeneous.  
 252 Also note that for both polar and equatorial coolings the amplitude of the outer boundary heat  
 253 flux heterogeneity (black) is slightly larger than that of the inner boundary (red).

Case	$\langle q_o \rangle$	$\langle q_i \rangle$	Outer cooling	$\langle q_o \rangle^{h/l}$	Inner cooling	$\langle q_o^* \rangle$	$\langle q_i^* \rangle$
1	0.61	0.72	Equatorial	-0.39	Equatorial	0.59	0.46
2	0.65	0.72	Equatorial	-0.19	Equatorial	0.37	0.32
3	0.71	0.86	Polar	0.13	Polar	0.22	0.09
4	0.78	0.89	Polar	0.08	Polar	0.15	0.06
5	0.60	0.67	Equatorial	-0.23	Equatorial	0.46	0.45
6	0.74	0.89	Polar	0.11	Quasi-polar	0.21	0.04
7	0.77	0.89	Polar	0.06	Mid latitudes	0.12	0.07
8	0.84	0.82	Intermediate	0.02	Equatorial	0.16	0.17
9	0.71	0.87	Polar	0.16	Polar	0.26	0.07
10	0.74	0.91	Polar	0.13	Mid latitudes	0.21	0.05
11	0.45	0.49	Equatorial	-0.47	Equatorial	0.91	0.83

Table 3: Time-average cooling patterns and amplitudes. Positive anomaly of equatorial/polar outer boundary heat flux is termed "Equatorial cooling"/"Polar cooling" respectively. Other quantities are defined in the text.

254 The magnitude of the tangent cylinder effect, measured by (11), is shown in Figs. 8c and  
 255 9c. For polar cooling the effect is weakly dependent on the control parameters, with a tendency  
 256 to converge to zero as the relative effect of rotation decreases on approach to the non-rotating  
 257 regime. In contrast, for equatorial cooling the tangent cylinder effect is stronger **and with the**  
 258 **magnitude of  $\langle q_o \rangle^{h/l}$  steadily increasing decreasing** with increasing inertia, **reflecting the**  
 259 **transition from dominance of axial convective rolls outside the tangent cylinder for the**  
 260 **lowest Rossby numbers to more turbulent conditions in the larger Rossby numbers.** The

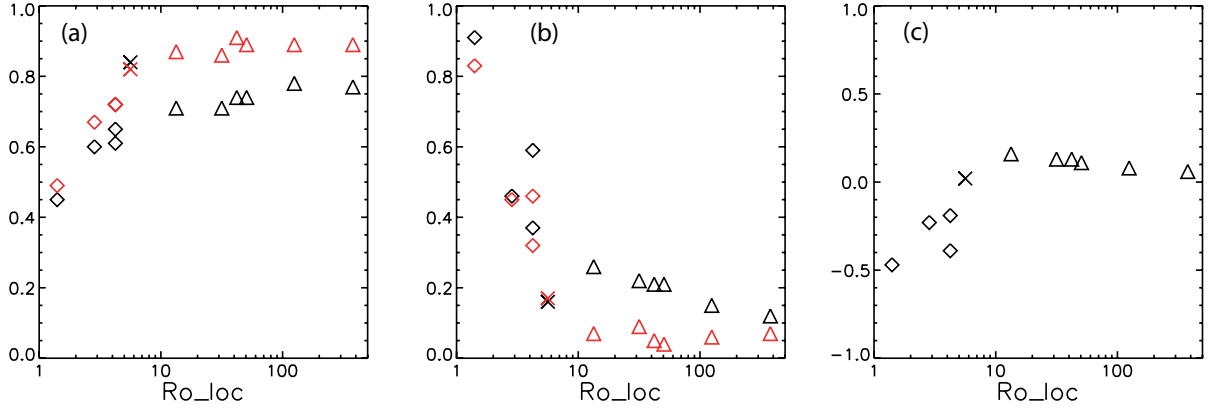


Figure 8: (a) Time-average non-dimensional mean outer boundary heat flux  $\langle q_o \rangle$  (black) and inner boundary heat flux  $\langle q_i \rangle$  (red), (b) amplitudes of the time-average outer boundary heat flux heterogeneity  $\langle q_o^* \rangle$  (black) and inner boundary heat flux heterogeneity  $\langle q_i^* \rangle$  (red), and (c) normalized difference between inside to outside tangent cylinder outer boundary heat flux, all as functions of the local convective Rossby number  $Ro_{loc}$  (15) in semi-log scale. Equatorial cooling is denoted by diamonds, polar cooling by triangles and intermediate cooling (case 8) by Xs. Note that the classification of symbols is based on the outer boundary heat flux patterns.

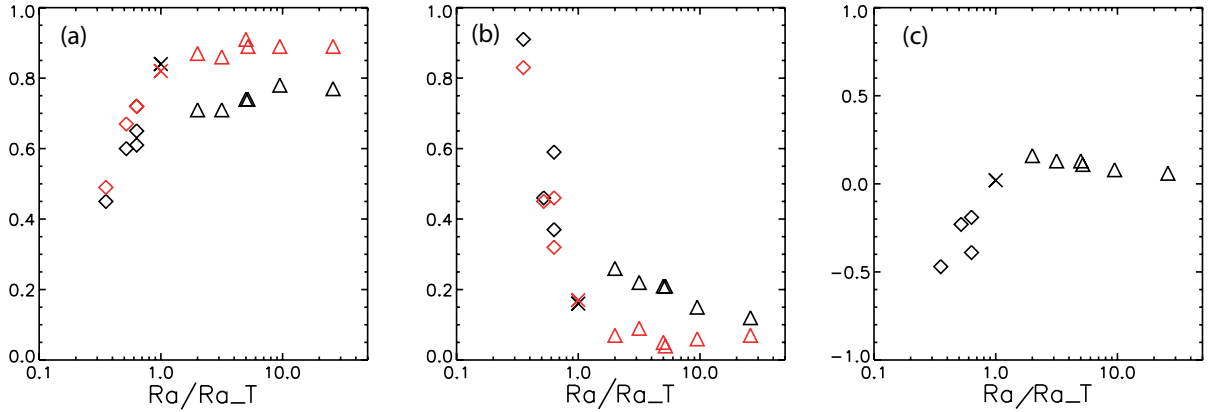


Figure 9: As in Fig. 8 but as functions of  $Ra/Ra_T$  (16).

261 largest tangent cylinder effect with polar cooling is registered in case 9 with  $\langle q_o \rangle^{h/l} = 0.16$ ,  
262 whereas in case 11 with equatorial cooling  $\langle q_o \rangle^{h/l} = -0.47$  (Table 3). The latter case with  
263 the lowest Ekman number (Table 2) also exhibits the lowest mean heat flux and the largest  
264 (relative) heterogeneity (Figs. 8-9).

265 In most cases the inner boundary heat flux shows a similar cooling pattern as the outer  
266 boundary heat flux, i.e. either polar cooling or equatorial cooling prevails in both (Table 3).  
267 However, this is not always precisely the case (see e.g. Fig. 6). In cases 7 and 10 polar  
268 cooling prevails on the outer boundary whereas the inner boundary is more small scale with  
269 a peak at mid latitudes vs. minima at the equator and the poles (which we classify as "mid  
270 latitudes" in Table 3), while in case 6 again polar cooling is observed on the outer boundary  
271 whereas the inner boundary is characterized by polar peak, equatorial low, but in addition  
272 low-latitude peaks (which we classify as "quasi polar" in Table 3). Overall, the a nearly z-  
273 invariant convection pattern is not expected to produce correlated heat flux patterns in the  
274 two boundaries, and such similarities probably arise due to thermal diffusion effects in the  
275 simulated thin shell. In realistic planetary conditions these diffusive effects are expected to be  
276 smaller (Aubert et al., 2007). Overall, the outer boundary heat flux seems to globally display  
277 larger scale patterns than the inner boundary heat flux.

## 278 **4 Dynamical regime for buried oceans**

279 Here we introduce possibly relevant parametric regimes. Fig. 10 presents the regime diagram  
280 of Gastine et al. (2016) (dashed grey curves) for convecting rotating flows in a spherical shell.  
281 The regime diagram is given in terms of the Ekman and Rayleigh numbers. At the onset of  
282 supercritical convection the flow is weakly non-linear. When the Rayleigh number exceeds  
283 six times the critical value for convection, three flow regimes are possible. For small Rayleigh  
284 numbers such that  $Ra < 0.4E^{-8/5}$  the flow resides in a rapidly rotating regime. For strongly  
285 convecting systems in which  $Ra > 100E^{-12/7}$  the flow is in a non-rotating regime. In between,  
286 a transitional regime prevails. For more details see Gastine et al. (2016).

287 We consider Titan's ocean as an emblematic example for our models (see section 5). In

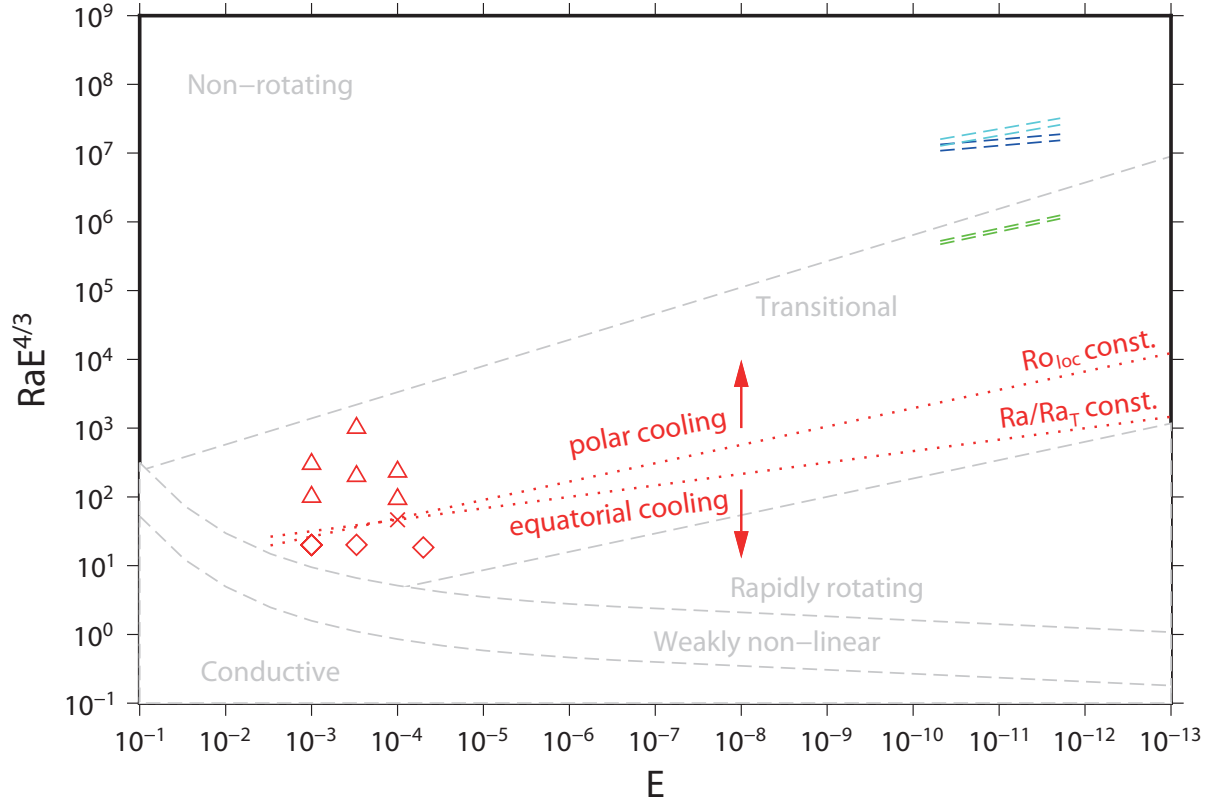


Figure 10: Parameter space for convecting rotating flows in a spherical shell with the example of Titan.  $E$  is the Ekman number (5) and  $Ra$  is the Rayleigh number (7).  $RaE^{4/3}$  is a measure of supercriticality of the Rayleigh number (Jones et al., 2000). The regime diagram obtained by Gastine et al. (2016) is reproduced by dashed grey lines. The parameter range corresponding to Titan’s ocean is denoted by dashed colored lines. The estimated range for the Ekman number corresponds to endmember values for the ocean thickness  $D$  (Vance et al., 2018). Values for the Rayleigh number are based on three estimates of the temperature scale  $\Delta T$  following the scaling for the non-rotating regime by Roche et al. (2010) (blue) and Gastine et al. (2015) (cyan) and the scaling for the rapidly rotating regime by Gastine et al. (2016) (green). For each of the three scaling laws, two lines correspond to the low and high heat flux values. The models presented in this study are denoted by red diamonds (equatorial cooling), red triangles (polar cooling) and red X (intermediate cooling). The **two** dotted red **lines** separating the equatorial and polar cooling regimes is **are** given by constant **values** of the local convective Rossby number **and**  $Ra/Ra_T$  of intermediate case 8 **respectively** (see Table 2). For more details see text.

288 order to estimate the appropriate Ekman and Rayleigh numbers for Titan’s ocean, we adopt  
 289 the models by Vance et al. (2018) to constrain its geometry. The extreme values for thickness,  
 290  $D = 91$  km (ocean with 10%  $\text{MgSO}_4$ , densest core) and 420 km (ocean with pure water, less  
 291 dense core), lead respectively to  $r_i/r_o = 0.96$  and 0.84. Assuming a viscosity  $\nu = 1.8 \cdot 10^{-6}$   
 292  $\text{m}^2\text{s}^{-1}$  and a given rotation rate  $\Omega = 4.6 \cdot 10^{-6} \text{ s}^{-1}$  at present, this range of values for  $D$  leads  
 293 to a relatively robust range for the Ekman number  $E = 1.9 \cdot 10^{-12} - 4.8 \cdot 10^{-11}$ .

294 Estimates of the Rayleigh number for Titan’s ocean are much less well constrained as it  
 295 further depends on other thermodynamical constants and crucially on the essentially unknown  
 296 temperature difference across the ocean  $\Delta T$ . This temperature difference can be derived from  
 297 the Nusselt-Rayleigh relation and an estimate of the heat flux at the top of the ocean,  $q_o$ . The  
 298 Nusselt number is defined as:

$$Nu = \frac{q_o D}{\rho C_p \kappa \Delta T}. \quad (17)$$

299 The extrapolation of  $Nu - Ra$  relation to very high Rayleigh numbers is, however, debatable  
 300 (e.g. Roche et al., 2010; Gastine et al., 2015). To obtain the Nusselt and Rayleigh numbers  
 301 relevant for Titan’s ocean, we first use two estimates of  $Nu - Ra$  relation proposed earlier for  
 302 the non-rotating regime:  $Nu = 0.07 \cdot Ra^{1/3}$  and  $Nu \propto Ra^{0.389}$ , derived from numerical simu-  
 303 lations (Gastine et al., 2015, cyan dashed lines in Fig. 10) and laboratory experiments (Roche  
 304 et al., 2010, blue dashed lines in Fig. 10) respectively. In particular, Roche et al. (2010) showed  
 305 that the  $Ra$  exponent increases for  $Ra > 7 \cdot 10^{11}$ , a regime that cannot be reached in numerical  
 306 simulations, from 0.33 to 0.389. For the second power law we obtain a prefactor 0.0171 by  
 307 assuming that the two laws predicted the same Nusselt number for a Rayleigh number equal  
 308 to  $10^{11}$ , i.e.  $Nu = 0.0171 \cdot Ra^{0.389}$ . We also consider the scaling relation corresponding to  
 309 rapidly-rotating convection (Gastine et al., 2016):  $Nu = 0.15 Ra^{3/2} E^2$  (green dashed lines in  
 310 Fig. 10).

311 Thermal evolution models predict that the power coming out of the rocky core of Titan  
 312 at present is between 450 and 600 GW (Tobie et al., 2006). This corresponds to an average  
 313 heat flux of about  $q_o = 6$  and  $8 \text{ mW/m}^2$  at the top of the ocean interface, assuming an ice  
 314 shell thickness of 75 – 100 km. These two values lead to the pairs of parallel dashed colored  
 315 lines in Fig. 10. For Titan’s ocean, we assume the following parameters: gravity  $g_0 = 1.35$

316 m/s<sup>2</sup>, thermal diffusivity  $\kappa = 1.3 \cdot 10^{-7}$  m<sup>2</sup>/s and thermal expansivity  $\alpha = 3.2 \cdot 10^{-4}$  K<sup>-1</sup>  
317 (cf. Choukroun et al., 2010). Using these values and assuming  $q_o = 6 - 8$  mW/m<sup>2</sup> and ocean  
318 thickness ranging between 90 and 450 km, the temperature difference across the ocean is  
319 between  $4 \cdot 10^{-4}$  and  $1.4 \cdot 10^{-3}$  K corresponding to Rayleigh numbers ranging between  $3 \cdot 10^{19}$   
320 (for  $D = 90$  km and  $q_o = 6$  mW/m<sup>2</sup> in the rapidly rotating case) and  $1.3 \cdot 10^{23}$  (for  $D = 450$   
321 km and  $q_o = 8$  mW/m<sup>2</sup> in the non-rotating case) (see Fig. 10).

322 Based on the above estimates Titan’s ocean most likely falls in either the non-rotating or  
323 the transitional regimes. Of these two, the non-rotating regime has been studied extensively  
324 (for a summary see Gastine et al., 2016). Furthermore, as will be shown below (section 5),  
325 observations suggest a significant latitudinal dependence of heat flux at the top of Titan’s ocean  
326 with a fair degree of equatorial symmetry (as proposed by Soderlund et al., 2014, for Europa),  
327 a feature that the asymptotic non-rotating regime shall not produce. We thus focused our  
328 analysis (section 2) on the less studied transitional regime, which is more promising in terms  
329 of latitudinal equatorially symmetric dynamics.

330 We obtained two main types of solutions (section 3), characterized by either larger outer  
331 boundary heat flux at low latitudes (which we term equatorial cooling and denote by red dia-  
332 monds in Fig. 10) or by larger outer boundary heat flux at high latitudes (which we term polar  
333 cooling and denote by red triangles in Fig. 10). An intermediate cooling case with a more  
334 complicated flow pattern is denoted by red X in Fig. 10. As can be seen in Fig. 10, all our flow  
335 models fall within the transitional regime of Gastine et al. (2016). ~~A constant value~~ **Constant**  
336 **values** of the local convective **various** Rossby numbers (see section 2) which correspond to  
337 our intermediate case separate the equatorial and polar cooling models (see dotted red **lines** in  
338 Fig. 10). ~~Note that this line is parallel to the line separating the rapidly rotating and transitional~~  
339 ~~regimes.~~

340 The aspect ratio in our simulations (mostly 0.8) corresponds to a slightly thicker shell than  
341 the upper estimate of Vance et al. (2018). Note that they proposed internal structures that are  
342 not fully satisfactory in the case of Titan, since the compositional models for the rock com-  
343 ponent do not match the density of the interior model (Vance et al., 2018). More importantly,  
344 while our models and those of Gastine et al. (2016) are essentially similar (simulations of ro-

345 tating convection of Boussinesq fluids), possible ~~shift~~ **shifts** of regime boundaries are expected  
346 between Titan’s ocean dynamics and the simulations of Gastine et al. (2016). In the latter, grav-  
347 ity varies as  $r^{-2}$  and the ratio  $r_i/r_o$  is set to 0.6, whereas in our simulations gravity is ~~uniform~~  
348 **varies as**  $r$  and the shell is thinner, both of which being probably more relevant choices for  
349 Titan’s ocean. **However, Mound and Davies (2017) found similar regime boundaries as**  
350 **Gastine et al. (2016) despite using different gravity profile, aspect ratio and boundary**  
351 **conditions. Whether this similarity holds for the non-accessible planetary parameters**  
352 **remains an open question.**

## 353 **5 Implications for the dynamics and structure of Titan’s hy-** 354 **dropshere**

355 Here we compare the cooling regimes in our dynamical models to the heat flux anomalies at  
356 the top of Titan’s ocean inferred from the analysis of topography and gravity data collected  
357 by the Cassini spacecraft (Kvorka et al., 2018). In Kvorka et al. (2018), Titan’s topography  
358 (Lorenz et al., 2013) and gravity field (Iess et al., 2012) are interpreted with a viscoelastic  
359 flow model taking into account deflection of the ice/ocean interface and heat transport by  
360 thermal conduction through the ice shell including both heterogenous heat source due to tidal  
361 heating inside the ice shell and heat flux anomalies from the ocean. Two models of topography-  
362 dependent erosion and deposition are considered: one where erosion is neglected (NE, no  
363 erosion) and another where it is accounted for in a simple manner (E). The average heat flux  
364 values derived with such an approach depend on several rheological parameters for the ice  
365 among which the grain size, assumed uniform, and a cut-off maximum value. For simplicity,  
366 we adopt here the reference values favored by Kvorka et al. (2018) that were used in their Figs.  
367 9 and 11.

368 Non-zonal effects might contribute to the global heat flux due to a heterogenous heat flux at  
369 the seafloor interface with a high-pressure ice mantle governing the specific dynamics of such  
370 a layer (Choblet et al., 2017b; Kalousová et al., 2018). Indeed in the two models proposed  
371 by Kvorka et al. (2018) the non-zonal contributions are larger than the zonal contributions, by  
372 factors 1.9 (E) and 3.3 (NE). Here we focus on the zonal part of the models of Kvorka et al.

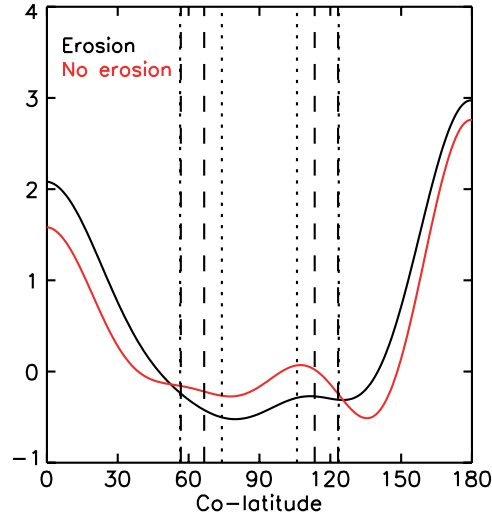


Figure 11: Zonal Zonally-averaged heat flux in  $\text{W/m}^2$  at the base of Titan's ice shell (Kvorka et al., 2018, see their Figs. 9 and 11) for models with (black) and without (red) erosion. Also indicated are plausible ranges for the latitude of the tangent cylinder at the base of the ice shell: vertical dashed lines based on Lefèvre et al. (2014) and vertical dotted lines based on Vance et al. (2018).

373 (2018) which may represent the internal dynamics in Titan's ocean.

374 Equatorial symmetry seems to dominate the zonal part of the heat flux models of Kvorka  
 375 et al. (2018), with largest heat flux in the polar regions of both hemispheres (Fig. 11). To  
 376 quantify this effect we decomposed the zonal heat flux  $q_o(\theta)$  to equatorially symmetric and  
 377 anti-symmetric parts by

$$q_o^s(\theta) = \frac{q_o(\theta) + q_o(\pi - \theta)}{2} \quad (18)$$

378 and

$$q_o^a(\theta) = q_o(\theta) - q_o^s(\theta) \quad (19)$$

379 where the superscripts  $s$  and  $a$  denote symmetric and anti-symmetric parts respectively, and  
 380  $\theta$  is in the northern hemisphere. Rms ratios of the equatorially anti-symmetric part to the  
 381 equatorially symmetric part  $\|q_o^a\|/\|q_o^s\|$  (where  $\|x\|$  denotes the rms of  $x$ ) for the two models  
 382 yield values of 0.19 (E) and 0.37 (NE). We interpret these high levels of equatorial symmetry  
 383 as a significant evidence that the rotating convecting dynamics highlighted in our simulations  
 384 might play a key role in Titan's ocean.

385 The values of spatial heterogeneity for Titan’s ocean are  $\langle q_o^* \rangle = 0.21$  for the model  
 386 without erosion (NE) and 0.30 for the model including erosion (E) (Kvorka et al., 2018). In  
 387 our models the values of spatial heterogeneity are  $\langle q_o^* \rangle \in [0.12 - 0.91]$  (Table 2), i.e. the  
 388 inferred values of for the spatial heterogeneity of Titan’s ocean heat flux are well within the  
 389 corresponding range in our simulations. Furthermore, if only values relevant for cases with  
 390 polar cooling are considered among our simulations, the range narrows down to  $[0.12, 0.26]$ ,  
 391 in very good agreement with the values inferred for Titan in the models by Kvorka et al. (2018).

392 The latitudinal dependence of the heat flux at the top of the ocean indeed reveals a pro-  
 393 nounced distribution of larger heat flux towards high latitudes (Fig. 11), i.e. polar cooling,  
 394 for both the (E) and (NE) models. Following the scaling argument derived above (**Figs. 8-9**  
 395 **and Table 3**), we anticipate that this noticeable feature could imply **either** a value of the local  
 396 Rossby number  $Ro_{loc}$  larger than  $\sim 10$  **or alternatively a value of  $Ra/Ra_T$  larger than  $\sim 1$ ,**  
 397 **both applied** for Titan’s ocean. Given the relatively well constrained estimates for the Ekman  
 398 number (cf. section 4,  $E \simeq 1.9 \cdot 10^{-12} - 4.8 \cdot 10^{-11}$ ), the definition of  $Ro_{loc}$  (15) implies  
 399 that the appropriate value for the Rayleigh number is larger than  $2.0 \cdot 10^{17} - 3.6 \cdot 10^{19}$ . **In**  
 400 **contrast, for the same  $E$  range the definition of  $Ra/Ra_T$  (16) implies a somewhat lower**  
 401 **range of values for the minimal Rayleigh number of  $3.0 \cdot 10^{16} - 3.8 \cdot 10^{18}$ . This range is**  
 402 **These lower bounds are** in agreement with the range derived above of  $Ra \simeq 10^{19} - 10^{25}$   
 403 (section 4), but hardly puts a constraint on it. A potentially stronger insight into the Rayleigh  
 404 number is derived considering that the polar cooling pattern indicates that Titan’s ocean lies in  
 405 the transitional regime depicted by Gastine et al. (2016) (Fig. 10), and not in the non-rotating  
 406 regime since the latter should not involve latitudinal dependence of the heat flux. If the bound-  
 407 ary between the two ( $Ra < 100E^{-12/7}$ ) is directly applied to the case of Titan’s ocean, its  
 408 Rayleigh number is smaller than  $4.9 \cdot 10^{19} - 1.2 \cdot 10^{22}$ , depending on the value for the Ekman  
 409 number.

410 Finally, while the latitude at which the tangent cylinder intersects the outer boundary of  
 411 Titan’s ocean cannot be constrained from Fig. 11 without ambiguity, we also note that con-  
 412 sidering the ocean thickness ranges proposed in the literature (e.g. Lefèvre et al., 2014; Vance  
 413 et al., 2018) allows to compute the ratio  $\langle q_o \rangle^{h/l}$  introduced in Eq. 11. For the thinnest shell  
 414 considered by Vance et al. (2018) of  $r_i/r_o = 0.96$  the latitude of the tangent cylinder is  $16^\circ$ ,

415 and the corresponding values for  $\langle q_o \rangle^{h/l}$  are 0.052 (E) and 0.016 (NE). For the thickest  
 416 shell of  $r_i/r_o = 0.83$  the latitude of the tangent cylinder is  $34^\circ$ , and the corresponding values  
 417 for  $\langle q_o \rangle^{h/l}$  are 0.073 (E) and 0.025 (NE). All these are positive ratios, indicating polar  
 418 cooling as expected. While the values for the model without erosion (NE) are slightly smaller  
 419 than the range observed in our simulations with polar cooling ( $[0.06, 0.16]$ ), the values for the  
 420 model with erosion (E) correspond to the lower end of this range. Together with its twice more  
 421 pronounced equatorial symmetry, this may indicate that the model with erosion (E) is a better  
 422 candidate for Titan's ice shell/ocean interaction. Note that the change of trend of the zonal  
 423 heat flux based on the models of Kvorka et al. (2018) occurs at higher latitudes than the tan-  
 424 gent cylinder (Fig. 11), in contrast to our self-consistent models in which the change of trend  
 425 in the zonal heat flux appears at somewhat lower latitudes than the tangent cylinder (Fig. 7).

## 426 6 Discussion

427 In Earth's liquid outer core, which is a thick shell with an aspect ratio of 0.35,  $E \ll 1$  and  
 428  $Ro \ll 1$  (e.g. Olson, 2007), hence rapid rotation effects are thought to prevail. Outside the tan-  
 429 gent cylinder, where the rotation and gravity vectors are nearly perpendicular, according to the  
 430 Taylor-Proudman theorem the flow is expected to be invariant in the direction parallel to the  
 431 rotation axis. This gives axial columns of fluid (e.g. Busse, 1970; Jault, 2008). Inside the tan-  
 432 gent cylinder, where the rotation and gravity vectors are nearly parallel, the thermo-chemical  
 433 wind balance gives spiraling flow with polar upwelling **structures** which are evident by ob-  
 434 served dispersed magnetic flux (Olson and Aurnou, 1999) though in a somewhat non-trivial  
 435 way (Cao et al., 2018). Competing rotation and convection effects determine the fluid dynam-  
 436 ics in the shell. **Close to the onset of convection** when rotation effects dominate, columnar  
 437 convection outside the tangent cylinder is more vigorous than thermal wind driven upwelling  
 438 inside the tangent cylinder, resulting in equatorial cooling. Conversely, when convection ef-  
 439 fects dominate, **these axial convective rolls are broken, convective plumes fill the tangent**  
 440 **cylinder and** the thermal wind driven polar upwelling results in polar cooling (Tilgner and  
 441 **Busse, 1997; Busse and Simitev, 2015). This effect is particularly significant with thin**  
 442 **shells in which the tangent cylinder occupies a much larger surficial fraction of the outer**

443 **boundary.**

444 This rationale was recently explored in the context of thin shells which are applicable  
445 for the buried oceans of icy moons. Miquel et al. (2018) simulated the dynamics in a thin,  
446 rapidly rotating shell using 3D numerical models as well as a non-hydrostatic equatorial  $\beta$ -  
447 plane convection model. In both cases they found that in the limit of rapid rotation (i.e.  $E \ll$   
448 1) convection is trapped at low latitudes and the peak heat flux appears at the equator (i.e.  
449 equatorial cooling). The latitudinal extent of the large equatorial heat flux is determined by  
450  $\epsilon/E$  where  $\epsilon^2 = D/r_o$  (Miquel et al., 2018).

451 Our results show that the competition between rotation and convection is well captured  
452 by the Rossby number, as was previously proposed (Soderlund et al., 2014). We find that  
453 equatorial cooling prevails when the models are closer to the rapidly ~~rotation~~ **rotating** regime,  
454 whereas polar cooling emerges when the models are closer to the non-rotating regime, in both  
455 cases within the transitional regime (Fig. 10) of Gastine et al. (2016). This parameter depen-  
456 dence of the latitudinal heat flux distribution is in agreement with previous studies (**Tilgner**  
457 **and Busse, 1997; Busse and Simitev, 2015**). For example, Busse and Simitev (2006) found in  
458 numerical dynamos with Earth-like geometry that increased rotation (i.e. lower  $E$ ) gives more  
459 enhanced equatorial cooling. Likewise, Yadav et al. (2016) found in both rotating convec-  
460 tion simulations and numerical dynamos that increased convection vigor (i.e. larger  $Ra$ ) gives  
461 more enhanced polar cooling. Miquel et al. (2018) found in asymptotically thin shell, rapidly  
462 rotating models equatorially trapped convection that gives peak equatorial cooling. Guervilly  
463 and Cardin (2017) studied zonal flows and heat transport in a quasi-geostrophic model which  
464 allows accessing very low Ekman numbers. They found that the equatorial cooling pattern is  
465 further enhanced by the rapidly rotating quasi-geostrophic flows because the convective trans-  
466 port is perpendicular to the rotation axis. In contrast, early models with moderate rotation  
467 and convection vigor found mixed polar and equatorial cooling (Gilman, 1975, 1977), while  
468 Aurnou et al. (2008) found polar cooling in a rapidly rotating, strongly convecting simulation.

469 The key to reconcile these results may be the role of zonal flows. According to the Taylor-  
470 Proudman theorem, axial convective columns emerge in rapidly rotating fluids. These cylin-  
471 drical flow structures are highly efficient in transporting heat in the equatorial region, hence

472 the resulting equatorial cooling on approach to the rapidly rotating regime (e.g. Busse and  
473 Simitev, 2006; Yadav et al., 2016; Guervilly and Cardin, 2017; Miquel et al., 2018). However,  
474 increased rotation may give rise to stronger zonal flows that tend to diminish the equatorial  
475 heat flux, which may lead to polar cooling (Aurnou et al., 2008). Such strong zonal flows are  
476 especially prominent under free-slip boundary conditions (Aurnou et al., 2008; Yadav et al.,  
477 2016) but may also emerge with no-slip boundary conditions. The zonal flow exhibits non-  
478 monotonic dependence on the Rossby number (Yadav et al., 2016) which may then explain  
479 these two contradicting parameter dependences of the outer boundary heat flux pattern. Addi-  
480 tional complications may arise due to dependences on e.g. the shell thickness and the Prandtl  
481 number.

482 In the context of Titan’s buried ocean, a new independent constraint is brought from the  
483 inferred heat flux models of Kvorka et al. (2018). These models clearly indicate that polar cool-  
484 ing prevails at the top of Titan’s ocean (Fig. 11). Assuming that this is true, we envision two  
485 possible interpretations. According to our models, Titan’s ocean is at the transitional regime  
486 close to the non rotating regime with relatively strong convection. In contrast, according to the  
487 model of Aurnou et al. (2008), convection in Titan’s ocean would be relatively weak and the  
488 dynamics would then be dominated by rotational effects, but strong zonal flows diminish the  
489 equatorial heat flux.

490 It is worth noting that the regime diagram (Fig. 10) of Gastine et al. (2016) was obtained  
491 using a fixed shell aspect ratio of 0.6 and fixed  $\Delta T$  boundary conditions. Different thermal  
492 boundary conditions (i.e. prescribed heat flux at one or both boundaries) or different shell  
493 thicknesses would likely require some updating of the scaling laws separating the different  
494 flow regimes. For example, our cases 1 and 2 have the same control parameters (hence overlap  
495 in Fig. 10) but different shell thicknesses (Table 2). Although both cases give equatorial  
496 cooling, the amplitude of  $\langle q_o \rangle^{h/l}$  in case 2 with the thinner shell is twice smaller (Table  
497 3), suggesting that (for given control parameters) a thinner shell favors polar cooling. In that  
498 respect replacing  $Ra$  by the convective power, which accounts for both the thermal boundary  
499 conditions and the shell geometry (Aubert et al., 2009), could be more appropriate. Other  
500 phenomena (e.g. compositional effects) might also induce biases. Nevertheless, qualitatively  
501 the diagram in Fig. 10 may provide a useful guidance for comparing numerical models and

502 natural bodies.

503 **Our choice of isothermal and impermeable boundary conditions is not necessarily**  
504 **the most physically relevant. The outer boundary of the ocean corresponds to a phase**  
505 **change. So does the inner boundary in the case where high-pressure polymorphs of ice**  
506 **form a layer beneath. In a situation where isothermal conditions are applied to mimic**  
507 **the melting-freezing boundary, the choice of a non-penetrative velocity condition is ques-**  
508 **tionable. Alternatively, slowly evolving convection in the surrounding solid ice layers may**  
509 **affect the latitudinal variations in heat flux at the top of the ocean. Dynamics in the**  
510 **high-pressure ice mantle below the ocean may give heterogenous heat flux at the seafloor**  
511 **(Choblet et al., 2017b; Kalousová et al., 2018), whereas solid-state convection in the ice**  
512 **shell above can induce significant temperature anomalies, even more so if latitudinal vari-**  
513 **ation in surface insolation induces planetary scale convective features with polar down-**  
514 **welling and equatorial upwelling (Weller et al., 2019). If the surrounding ice shells can**  
515 **indeed support slowly varying large lateral temperature variations, then the more ap-**  
516 **propriate thermal boundary conditions for the ocean could be prescribed heterogeneous**  
517 **flux.**

518 While our main planetary target here is Titan, other ocean worlds would likely correspond  
519 to other regions in the regime diagram. Considering an average value for the ocean thickness  
520 of 40 km, Enceladus displays an Ekman number and geometry comparable to Titan's:  $E \simeq$   
521  $2.2 \cdot 10^{-11}$  and  $r_i/r_o = 0.83$ . A plausible range for Enceladus' ocean Rayleigh number involves  
522 however significantly lower values than Titan's:  $Ra \simeq 5 \cdot 10^{17} - 10^{21}$ . This would in theory  
523 imply that the appropriate range for Enceladus' ocean lies exclusively in the transitional regime  
524 with equatorial cooling as a possibility. However, because Enceladus' ice shell is more than  
525 three times thicker near the equator than near the poles (Čadek et al., 2016; Beuthe et al.,  
526 2016; Le Gall et al., 2017) and internal heating in the ice shell is negligible (Čadek et al.,  
527 2019), equatorial cooling is unlikely for its ocean. Furthermore, the actual heat flux pattern  
528 at the top of Enceladus' ocean may be dominated by polar cooling due to forcing coming  
529 from its core (Choblet et al., 2017a). Overall, various complexities (non spherical container,  
530 strongly heterogeneous bottom heat flux) should be considered for some planetary objects.  
531 Given the variety of sizes and orbital characteristics, distinct dynamical regimes are expected

532 for subsurface oceans of icy moons.

533 As acknowledged by Kvorka et al. (2018), inaccurate topography and gravity measure-  
534 ments render their derived heat flux models uncertain. It is therefore probably premature to  
535 draw definite conclusions from the comparison exercise between Titan's heat flux inferred  
536 from observations and our simulated heat flux at the top of the shell. Nevertheless, we con-  
537 sider that the overall agreement in terms of pattern and amplitude is encouraging for both  
538 approaches. This also highlights the importance of future geophysical observations by space  
539 missions which may further constrain the dynamics of deep oceans.

## 540 **Acknowledgments**

541 This work acknowledges the financial support from Région Pays de la Loire, project Geo-  
542 PlaNet (convention N° 2016-10982). We also acknowledge support from CNES JUICE and  
543 Europa Clipper. We are grateful to Krista Soderlund **and Thomas Gastine** for insightful dis-  
544 cussions that enriched this paper.

## References

- 546 Amit, H., Choblet, G., 2009. Mantle-driven geodynamo features - effects of post-Perovskite  
547 phase transition. *Earth Planets Space* 61, 1255–1268.
- 548 Amit, H., Choblet, G., Olson, P., Monteux, J., Deschamps, F., Langlais, B., Tobie, G., 2015.  
549 Towards more realistic core-mantle boundary heat flux patterns: a source of diversity in  
550 planetary dynamos. *Prog. Earth Planet. Sci.* 2:26, DOI: 10.1186/s40645-015-0056-3.
- 551 Aubert, J., Amit, H., Hulot, G., 2007. Detecting thermal boundary control in surface flows  
552 from numerical dynamos. *Phys. Earth Planet. Inter.* 160, 143–156.
- 553 Aubert, J., Amit, H., Hulot, G., Olson, P., 2008. Thermo-chemical wind flows couple Earth's  
554 inner core growth to mantle heterogeneity. *Nature* 454, 758–761.
- 555 Aubert, J., Gastine, T., Fournier, A., 2017. Spherical convective dynamos in the rapidly rotating  
556 asymptotic regime. *J. Fluid. Mech.* 813, 558–593.
- 557 Aubert, J., Labrosse, S., Poitou, C., 2009. Modelling the paleo-evolution of the geodynamo.  
558 *Geophys. J. Int.* 179, 1414–1428.
- 559 Aurnou, J., Heimpel, M., Allem, L., King, E., Wicht, J., 2008. Convective heat transfer and  
560 the pattern of thermal emission on the gas giants. *Geophys. J. Int.* 173, 793–801.
- 561 Aurnou, J. M., Calkins, M. A., Cheng, J. S., King, E. M., Nieves, D., Soderlund, K. M.,  
562 Stellmach, S., 2015. Rotating convective turbulence in Earth and planetary cores. *Phys.*  
563 *Earth Planet. Inter.* 246, 52–71.
- 564 Baland, R.-M., Tobie, G., Lefèvre, A., Van Hoolst, T., 2014. Titan's internal structure inferred  
565 from its gravity field, shape, and rotation state. *Icarus* 237, 29–41.
- 566 Baland, R.-M., Van Hoolst, T., Yseboodt, M., Karatekin, O., 2011. Titan's obliquity as evi-  
567 dence of a subsurface ocean? *Astronom. Astrophys.* 530, A141.
- 568 Béghin, C., Randriamboarison, O., Hamelin, M., Karkoschka, E., Sotin, C., Whitten, R. C.,  
569 Berthelier, J.-J., Grard, R., Simões, F., 2012. Analytic theory of Titan's Schumann res-

570 onance: Constraints on ionospheric conductivity and buried water ocean. *Icarus* 218(2),  
571 1028–1042.

572 Béghin, C., Sotin, C., Hamelin, M., 2010. Titan’s native ocean revealed beneath some 45km  
573 of ice by a Schumann-like resonance. *Comp. Rend. Geosci.* 342, 425–433.

574 Beuthe, M., Rivoldini, A., Trinh, A., 2016. Enceladus’s and Dione’s floating ice shells sup-  
575 ported by minimum stress isostasy. *Geophys. Res. Lett.* 43(19), 10088–10096.

576 Busse, F., 1970. Thermal instabilities in rapidly rotating systems. *J. Fluid Mech.* 44, 441–460.

577 Busse, F., Simitev, R., 2006. Parameter dependences of convection-driven dynamos in rotating  
578 spherical fluid shells. *Geophys. Astrophys. Fluid Dyn.* 100, 341–361.

579 Busse, F. H., Simitev, R. D., 2015. Planetary dynamos. In: Spohn, T. (Ed.), *Treatise on Geo-*  
580 *physics*. Vol. 10. Elsevier Science.

581 Čadek, O., Souček, O., Běhounková, M., Choblet, G., Tobie, G., Hron, J., 2019. Long-term  
582 stability of Enceladus’ uneven ice shell. *Icarus* 319, 476–484.

583 Čadek, O., Tobie, G., Van Hoolst, T., Massé, M., Choblet, G., Lefèvre, A., Mitri, G., Baland,  
584 R.-M., Běhounková, M., Bourgeois, O., et al., 2016. Enceladus’s internal ocean and ice  
585 shell constrained from Cassini gravity, shape, and libration data. *Geophys. Res. Lett.* 43,  
586 5653–5660.

587 Cao, H., Yadav, R. K., Aurnou, J., 2018. Geomagnetic polar minima do not arise from steady  
588 meridional circulation. *Proc. Nat. Acad. Sci.* 115 (44), 11186–11191.

589 Choblet, G., Tobie, G., Sotin, C., Běhounková, M., Čadek, O., Postberg, F., Souček, O., 2017a.  
590 Powering prolonged hydrothermal activity inside Enceladus. *Nature Astro.* 1(12), 841.

591 Choblet, G., Tobie, G., Sotin, C., Kalousova, K., Grasset, O., 2017b. Heat transport in the  
592 high-pressure ice mantle of large icy moon. *Icarus* 285, 252–262.

593 Choukroun, M., Grasset, O., Tobie, G., Sotin, C., 2010. Stability of methane clathrate hydrates  
594 under pressure: Influence on outgassing processes of methane on Titan. *Icarus* 205, 581–  
595 593.

- 596 Dormy, E., Soward, A. M., Jones, C. A., Jault, D., Cardin, P., 2004. The onset of thermal  
597 convection in rotating spherical shells. *J. Fluid Mech.* 501, 43–70.
- 598 Dziewonski, A. M., Anderson, D. L., 1981. Preliminary reference Earth model. *Phys. Earth*  
599 *Planet. Inter.* 25, 297–356.
- 600 Gabasova, L. R., Tobie, G., Choblet, G., 2018. Compaction-driven evolution of Pluto’s rocky  
601 core: Implications for water-rock interactions. In: *Ocean Worlds*. Vol. 20185.
- 602 Gastine, T., Wicht, J., Aubert, J., 2016. Scaling regimes in spherical shell rotating convection.  
603 *J. Fluid. Mech.* 808, 690–732.
- 604 Gastine, T., Wicht, J., Aurnou, J., 2015. Turbulent Rayleigh-bénard convection in spherical  
605 shells. *J. Fluid Mech.* 778, 721–764.
- 606 Gilman, P., 1975. Linear simulations of boussinesq convection in a deep rotating spherical  
607 shell. *J. Atmos. Sci.* 32, 1331–1352.
- 608 Gilman, P., 1977. Nonlinear dynamics of Boussinesq convection in a deep rotating shell—I.  
609 *Geophys. Astrophys. Fluid Dyn.* 8, 93–135.
- 610 Glatzmaier, G., 2002. Geodynamo simulations: how realistic are they? *Annu. Rev. Earth*  
611 *Planet. Sci. Lett.* 30, 237–257.
- 612 Goodman, J. C., Collins, G. C., Marshall, J., Pierrehumbert, R. T., 2004. Hydrothermal plume  
613 dynamics on Europa: Implications for chaos formation. *J. Geophys. Res.* 109(E3).
- 614 Grasset, O., Dougherty, M., Coustenis, A., Bunce, E., Erd, C., Titov, D., Blanc, M., Coates, A.,  
615 Drossart, P., Fletcher, L., et al., 2013. Jupiter icy moons explorer (JUICE): An ESA mission  
616 to orbit Ganymede and to characterise the Jupiter system. *Plan. Space Sci.* 78, 1–21.
- 617 Guervilly, C., Cardin, P., 2017. Multiple zonal jets and convective heat transport barriers in a  
618 quasi-geostrophic model of planetary cores. *Geophys. J. Int.* 211, 455–471.
- 619 Hauck, S. A., Mazarico, E., Padovan, S., Peale, S. J., 2018. Mercury’s internal structure. In:  
620 Solomon, S. C., Anderson, B. J., Nittler, L. R. (Eds.), *Mercury - The View after MESSEN-*  
621 *GER*. Cambridge Planetary Science.

- 622 Heimpel, M., Evans, M., 2013. Testing the geomagnetic dipole and reversing dynamo models  
623 over Earth's cooling history. *Phys. Earth Planet. Inter.* 224, 124–131.
- 624 Hemingway, D., Iess, L., Tajeddine, R., Tobie, G., 2018. The interior of Enceladus. In: Schenk,  
625 P. M. e. a. (Ed.), *Enceladus and the icy moons of Saturn*. Univ. of Arizona, Tucson.
- 626 Hsu, H.-W., Postberg, F., Sekine, Y., Shibuya, T., Kempf, S., Horanyi, M., Juhász, A., Al-  
627 tobelli, N., Suzuki, K., Masaki, Y., Kuwatani, T., Tachibana, S., Sirono, S.-I., Moragas-  
628 Klostermeyer, G., Srama, R., 2015. Ongoing hydrothermal activities within Enceladus. *Nature*  
629 519, 207–210.
- 630 Hsu, H.-W., Schmidt, J., Kempf, S., Postberg, F., Moragas-Klostermeyer, G., Seiß, M., Hoff-  
631 mann, H., Burton, M., Ye, S., Kurth, W. S., Horányi, M., Khawaja, N., Spahn, F. e. a., 2018.  
632 In situ collection of dust grains falling from Saturn's rings into its atmosphere. *Science* 362,  
633 doi:10.1126/science.aat3185.
- 634 Iess, L., Jacobson, R., Ducci, M., Stevenson, D., Lunine, J. I., Armstrong, J. W., Asmar, S.,  
635 Racioppa, P., Rappaport, N. J., Tortora, P., 2012. The tides of Titan. *Science* 337, 457–459.
- 636 Iess, L., Rappaport, N. J., Jacobson, R. A., Racioppa, P., Stevenson, D. J., Tortora, P., Arm-  
637 strong, J. W., Asmar, S. W., 2010. Gravity field, shape, and moment of inertia of Titan.  
638 *Science* 327, 1367–1369.
- 639 Jault, D., 2008. Axial invariance of rapidly varying diffusionless motions in the Earth's core  
640 interior. *Geophys. J. Int.* 166, 67–76.
- 641 Jones, C., Soward, A., Mussa, A., 2000. The onset of thermal convection in a rapidly rotating  
642 sphere. *J. Fluid Mech.* 405, 157–179.
- 643 Kalousová, K., Sotin, C., Choblet, G., Tobie, G., Grasset, O., 2018. Two-phase convection  
644 in Ganymede's high-pressure ice layer-implications for its geological evolution. *Icarus* 299,  
645 133–147.
- 646 Khurana, K. K., Kivelson, M. G., Russell, C. T., 2002. Searching for liquid water in Europa  
647 by using surface observatories. *Astrobiology* 2(1), 93–103.

- 648 Kirk, R., Stevenson, D., 1987. Thermal evolution of a differentiated Ganymede and implica-  
649 tions for surface features. *Icarus* 69(1), 91–134.
- 650 Kivelson, M., Khurana, K., 2002. The permanent and inductive magnetic moments of  
651 Ganymede. *Icarus* 157(2), 507–522.
- 652 Kvorka, J., Čadek, O., Tobie, G., Choblet, G., 2018. Does Titan’s long-wavelength topography  
653 contain information about subsurface ocean dynamics? *Icarus* 310, 149–164.
- 654 Le Gall, A., Leyrat, C., Janssen, M. A., Choblet, G., Tobie, G., Bourgeois, O., Lucas, A.,  
655 Sotin, C., Howett, C., Kirk, R., et al., 2017. Thermally anomalous features in the subsurface  
656 of Enceladus’s south polar terrain. *Nature Astro.* 1(4), 0063.
- 657 Lefèvre, A., Tobie, G., Choblet, G., Čadek, O., 2014. Structure and dynamics of Titan’s outer  
658 icy shell constrained from Cassini data. *Icarus* 237, 16–28.
- 659 Ligier, N., Poulet, F., Carter, J., Brunetto, R., Gourgéot, F., 2016. Vlt/sinfoni observations of  
660 Europa: New insights into the surface composition. *Astronom. J.* 151:163.
- 661 Lorenz, R. D., Stiles, B. W., Aharonson, O., Lucas, A., Hayes, A. G., Kirk, R. L., Zebker,  
662 H. A., Turtle, E. P., Neish, C. D., Stofan, E. R., et al., 2013. A global topographic map of  
663 Titan. *Icarus* 225(1), 367–377.
- 664 McCord, T. B., Teeter, G., Hansen, G. B., Sieger, M. T., Orlando, T. M., 2002. Brines exposed  
665 to Europa surface conditions. *J. Geophys. Res.* 107, E1, 5004.
- 666 Miquel, B., Xie, J.-H., Featherstone, N., Julien, K., Knobloch, E., 2018. Equatorially trapped  
667 convection in a rapidly rotating shallow shell. *Phys. Rev. Fluids* 3, 053801.
- 668 Mitri, G., Meriggiola, R., Hayes, A., Lefèvre, A., Tobie, G., Genova, A., Lunine, J. I., Zebker,  
669 H., 2014. Shape, topography, gravity anomalies and tidal deformation of Titan. *Icarus* 236,  
670 169–177.
- 671 Mound, J. E., Davies, C. J., 2017. Heat transfer in rapidly rotating convection with heteroge-  
672 neous thermal boundary conditions. *J. Fluid Mech.* 828, 601–629.

673 Nimmo, F., Pappalardo, R., 2016. Ocean worlds in the outer solar system. *J. Geophys. Res.*  
674 121(8), 1378–1399.

675 Ojakangas, G. W., Stevenson, D. J., 1989. Thermal state of an ice shell on Europa. *Icarus*  
676 81(2), 220–241.

677 Olson, P., 2007. Overview. In: Olson, P. (Ed.), *Treatise on Geophysics*. Vol. 8. Elsevier Science.

678 Olson, P., Aurnou, J., 1999. A polar vortex in the Earth’s core. *Nature* 402, 170–173.

679 Olson, P., Christensen, U., 2002. The time averaged magnetic field in numerical dynamos with  
680 nonuniform boundary heat flow. *Geophys. J. Int.* 151, 809–823.

681 Phillips, C. B., Pappalardo, R. T., 2014. Europa Clipper mission concept: Exploring Jupiter’s  
682 ocean moon. *Eos Trans. AGU* 95(20), 165–167.

683 Postberg, F., Kempf, S., Schmidt, J., Brilliantov, N., Beinsen, A., Abel, B., Buck, U., Srama,  
684 R., 2009. Sodium salts in E-ring ice grains from an ocean below the surface of Enceladus.  
685 *Nature* 459(7250), 1098.

686 Postberg, F., Schmidt, J., Kempf, S., Hillier, S., Srama, R., 2011. A salt-water reservoir as the  
687 source of a compositionally stratified plume on Enceladus. *Nature* 474, 620–622.

688 Roche, P.-E., Gauthier, F., Kaiser, R., Salort, J., 2010. On the triggering of the ultimate regime  
689 of convection. *New J. Phys.* 12, 085014.

690 Saur, J., Duling, S., Roth, L., Jia, X., Strobel, D. F., Feldman, P. D., Christensen, U. R., Rether-  
691 ford, K. D., McGrath, M. A., Musacchio, F., et al., 2015. The search for a subsurface ocean  
692 in Ganymede with Hubble space telescope observations of its auroral ovals. *J. Geophys.*  
693 *Res.* 120(3), 1715–1737.

694 Schaeffer, N., 2013. Efficient spherical harmonic transforms aimed at pseudo-spectral numer-  
695 ical simulations. *Geochem. Geophys. Geosyst.* 14, 751–758.

696 Schaeffer, N., Jault, D., Nataf, H.-C., Fournier, A., 2017. Turbulent geodynamo simulations: a  
697 leap towards Earth’s core. *Geophys. J. Int.* 211, 1–29.

- 698 Soderlund, K. M., Schmidt, B. E., Wicht, J., Blankenship, D. D., 2014. Ocean-driven heating  
699 of Europa's icy shell at low latitudes. *Nature Geosci.* 7, 16–19.
- 700 Tajeddine, R., Rambaux, N., Lainey, V., Charnoz, S., Richard, A., Rivoldini, A., Noyelles,  
701 B., 2014. Constraints on Mimas' interior from Cassini ISS libration measurements. *Science*  
702 346(6207), 322–324.
- 703 Taylor, G., 1917. Motion of solids in fluids when the flow is not irrotational. *Proc. R. Soc.*  
704 *Lond. A.* 93, 92–113.
- 705 Thomas, P., Tajeddine, R., Tiscareno, M., Burns, J., Joseph, J., Loredó, T., Helfenstein, P.,  
706 Porco, C., 2016. Enceladus's measured physical libration requires a global subsurface ocean.  
707 *Icarus* 264, 37–47.
- 708 Thomson, R. E., Delaney, J. R., 2001. Evidence for a weakly stratified European ocean sustained  
709 by seafloor heat flux. *J. Geophys. Res.* 106(E6), 12355–12365.
- 710 Tilgner, A., Busse, F. H., 1997. Finite-amplitude convection in rotating spherical fluid shells.  
711 *J. Fluid Mech.* 332, 359–376.
- 712 Tobie, G., Lunine, J. I., Sotin, C., 2006. Episodic outgassing as the origin of atmospheric  
713 methane on Titan. *Nature* 440, 61–64.
- 714 Vance, S., Brown, J., 2005. Layering and double-diffusion style convection in Europa's ocean.  
715 *Icarus* 177(2), 506–514.
- 716 Vance, S., Goodman, J., 2009. Oceanography of an ice-covered moon. *Europa*, 459–484.
- 717 Vance, S. D., Panning, M. P., Stähler, S., Cammarano, F., Bills, B. G., Tobie, G., Kamata, S.,  
718 Kedar, S., Sotin, C., Pike, W. T., et al., 2018. Geophysical investigations of habitability in  
719 ice-covered ocean worlds. *J. Geophys. Res.* 123(1), 180–205.
- 720 Vidal, J., Schaeffer, N., 2015. Quasi-geostrophic modes in the Earth's fluid core with an outer  
721 stably stratified layer. *Geophys. J. Int.* 202, 2182–2193.

- 722 Weller, M. B., Fuchs, L., Becker, T. W., Soderlund, K. M., 2019. Convection in thin shells  
723 of icy satellites: Effects of latitudinal surface temperature variations. *J. Geophys. Res.*, in  
724 press.
- 725 Wicht, J., 2002. Inner-core conductivity in numerical dynamo simulations. *Phys. Earth Planet.*  
726 *Inter.* 132, 281–302.
- 727 Yadav, R., Gastine, T., Christensen, U., Duarte, L., Reiners, A., 2016. Effect of shear and mag-  
728 netic field on the heat-transfer efficiency of convection in rotating spherical shells. *Geophys.*  
729 *J. Int.* 204, 1120–1133.
- 730 Zhang, K., Jones, C. A., 1993. The influence of Ekman boundary layers on rotating convection.  
731 *Geophys. Astrophys. Fluid Dyn.* 71, 145–162.
- 732 Zimmer, C., Khurana, K. K., Kivelson, M. G., 2000. Subsurface oceans on Europa and Cal-  
733 listo: Constraints from Galileo magnetometer observations. *Icarus* 147(2), 329–347.